

KEK Preprint 2012-21  
August 2012  
A/H

# A CLIC-Prototype Higgs Factory

R. BELUSEVIC and T. HIGO

*High Energy Accelerator Research Organization (KEK)*  
1-1 Oho, Tsukuba, Ibaraki 305-0801, Japan  
belusev@post.kek.jp

# Contents

<b>1</b>	<b>The Standard Model of particle physics</b>	<b>3</b>
<b>2</b>	<b>The Higgs mechanism</b>	<b>4</b>
<b>3</b>	<b>Recent discovery of a Higgs-boson candidate at LHC</b>	<b>6</b>
<b>4</b>	<b>Single Higgs production in <math>\gamma\gamma</math> collisions</b>	<b>7</b>
<b>5</b>	<b>Single Higgs production in <math>e^+e^-</math> annihilations</b>	<b>9</b>
<b>6</b>	<b>Higgs-pair production in <math>\gamma\gamma</math> and <math>e^+e^-</math> collisions</b>	<b>10</b>
<b>7</b>	<b>Higgs couplings to SM particles</b>	<b>13</b>
<b>8</b>	<b>The proposed facility in brief</b>	<b>15</b>
<b>9</b>	<b>The X-band accelerator complex</b>	<b>16</b>
<b>10</b>	<b>The RF system</b>	<b>18</b>
<b>11</b>	<b>Photon collider</b>	<b>19</b>
<b>12</b>	<b>Laser system for an X-band machine</b>	<b>21</b>
<b>13</b>	<b>Interaction region and beam dump</b>	<b>21</b>
<b>14</b>	<b>Luminosity and backgrounds at a <math>\gamma\gamma</math> collider</b>	<b>23</b>
<b>15</b>	<b>Main advantages over a TESLA-type design</b>	<b>25</b>
<b>16</b>	<b>Summary and Acknowledgements</b>	<b>25</b>

## References

**Abstract:** We propose that a pair of electron linacs with high accelerating gradients and an optical FEL be built at an existing laboratory. The linacs would employ CLIC-type rf cavities and a klystron-based power source; a two-beam scheme could be implemented at a later stage. The proposed facility would serve primarily as an  $e^+e^-/\gamma\gamma$  Higgs-boson factory. The rich set of final states in  $e^+e^-$  and  $\gamma\gamma$  collisions would play an essential role in measuring the mass, spin, parity, two-photon width and trilinear self-coupling of the Higgs boson, as well as its couplings to fermions and gauge bosons. These quantities are more difficult to determine with only one initial state. For some processes within and beyond the Standard Model, the required CM energy is considerably lower at the proposed facility than at an  $e^+e^-$  or proton collider.

## 1 The Standard Model of particle physics

Enormous progress has been made in the field of high-energy physics over the past five decades. The existence of a subnuclear world of quarks and leptons, whose dynamics can be described by quantum field theories possessing gauge symmetry (*gauge theories*), has been firmly established. The *Standard Model* (SM) of particle physics gives a coherent quantum-mechanical description of electromagnetic, weak and strong interactions based on fundamental constituents — quarks and leptons — interacting via force carriers — photons, W and Z bosons, and gluons.

The Standard Model is supported by two theoretical ‘pillars’: the *gauge principle* and the *Higgs mechanism* for particle mass generation. Whereas the former has been firmly established through precision electroweak measurements, the latter is yet to be fully tested.

In the SM, where electroweak symmetry is broken by the Higgs mechanism, the mass of a particle depends on its interaction with the Higgs field, a medium that permeates the universe. The photon and the gluon do not have such couplings, and so they remain massless. The Standard Model predicts the existence of a neutral spin-0 particle associated with the Higgs field, but it does not predict its mass. Although the existence of a Higgs field provides a simple mechanism for electroweak symmetry breaking, *our inability to predict the mass of the Higgs boson reflects the fact that we really do not understand at a fundamental level why this phenomenon occurs*. Another undesirable feature of the Standard Model is the *ad hoc* way in which fermion masses are introduced.

All of the couplings of the Higgs particle to gauge bosons and fermions are completely determined in the Standard Model in terms of electroweak coupling constants and fermion masses. Higgs production and decay processes can be computed in the SM unambiguously in terms of the Higgs mass alone. Since the coupling of the Higgs boson to fermions and gauge bosons is proportional to the particle masses (see Fig. 1), the Higgs boson will be produced in association with heavy particles and will decay into the heaviest particles that are kinematically accessible.

The rich set of final states in  $e^+e^-$  and  $\gamma\gamma$  collisions would play an essential role in measuring the mass ( $m_H$ ), spin, parity, two-photon width and trilinear self-coupling of the Higgs boson, as well as its couplings to fermions and gauge bosons; these quantities are more difficult to determine with only one initial state.

The Higgs-boson mass affects the values of electroweak observables through radiative corrections. The precision electroweak data obtained over the past three decades consists of over a thousand individual measurements. Many of those measurements may be combined to provide a global test of consistency with the SM. The best constraint on  $m_H$  is obtained by making a global

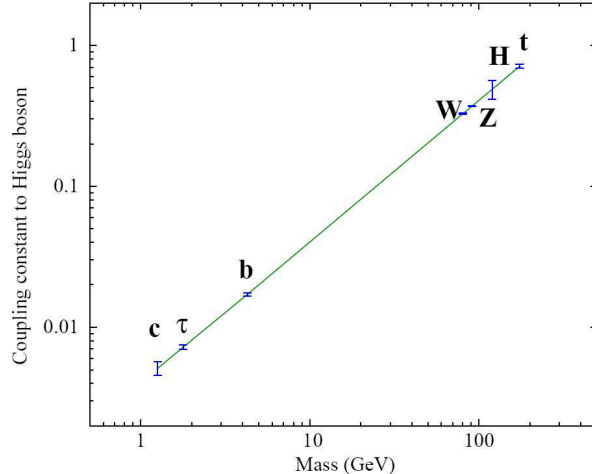


Figure 1: Precision with which the couplings of the Higgs particle with  $m_{\text{H}} = 120$  GeV can be determined at an  $e^+e^-$  collider with  $\int L = 500 \text{ fb}^{-1}$ . The coupling  $\kappa_i$  of the particle  $i$  with mass  $m_i$  is defined so that the relation  $m_i = v\kappa_i$  with  $v \simeq 246$  GeV holds in the SM [1].

fit to the electroweak data. Such a fit strongly suggests that the most likely mass for the SM Higgs boson is just above the limit of 114.4 GeV set by direct searches at the LEP  $e^+e^-$  collider [2].

The solid ellipse in Fig. 2 indicates the direct measurement of the W mass,  $m_{\text{W}}$ , and the top-quark mass,  $m_t$ . The dashed ellipse represents the indirect constraints between the two masses. Also shown is the correlation between  $m_{\text{W}}$  and  $m_t$  as expected in the Standard Model for different values of the Higgs-boson mass  $m_{\text{H}}$  (the diagonal band). Notice that the two ellipses overlap near the lines of constant  $m_{\text{H}}$ . This indicates that the Standard Model is a fairly good approximation to reality. Both ellipses are consistent with a low value of the Higgs-boson mass.

High-precision electroweak measurements, therefore, provide a natural complement to direct studies of the Higgs sector. All the measurements made at LEP and SLC could be repeated at the proposed facility using 90% polarized electron beams and at much higher luminosities. Assuming a geometric luminosity  $L_{e^+e^-} \approx 5 \times 10^{33} \text{ cm}^{-2} \text{ s}^{-1}$  at the Z resonance, about  $2 \times 10^9$  Z bosons can be produced in an operational year of  $10^7$  s. This is about 200 times the entire LEP statistics. Moreover, about  $10^6$  W bosons can be produced near the W-pair threshold at the optimal energy point for measuring the W-boson mass. An increase in the number of Z events by two orders of magnitude as compared to LEP data, and a substantially improved accuracy in the measurement of W-boson properties, would provide new opportunities for high-precision electroweak studies [3].

## 2 The Higgs mechanism

In order to provide a mechanism for the generation of particle masses in the *Standard Model* without violating its gauge invariance, a complex scalar SU(2) doublet  $\Phi$  with four real fields and *hypercharge*  $Y = 1$  is introduced. The dynamics of the field  $\Phi$  is described by the Lagrangian

$$\mathcal{L}_{\Phi} = (D_{\mu}\Phi)^{\dagger}(D^{\mu}\Phi) - \mu^2\Phi^{\dagger}\Phi - \lambda(\Phi^{\dagger}\Phi)^2 \quad (1)$$

where  $(D_{\mu}\Phi)^{\dagger}(D^{\mu}\Phi)$  is the kinetic-energy term and  $\mu^2\Phi^{\dagger}\Phi + \lambda(\Phi^{\dagger}\Phi)^2$  is the Higgs self-interaction potential. In the so-called *unitary gauge*,

$$\Phi = \frac{1}{\sqrt{2}} \begin{pmatrix} 0 \\ v + \text{H} \end{pmatrix} \quad (2)$$

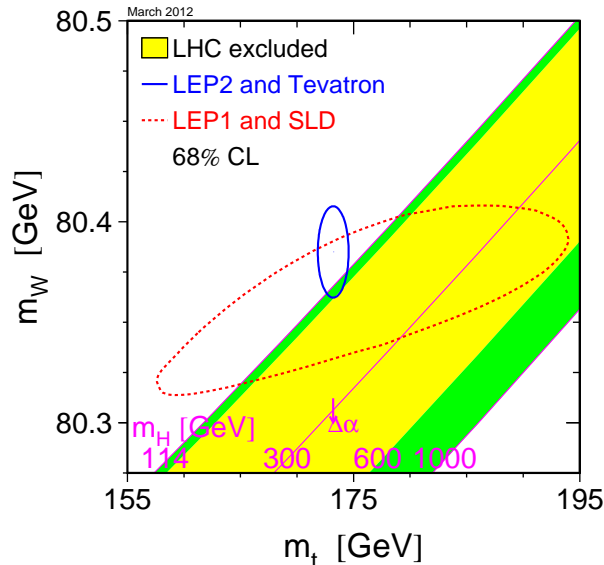


Figure 2: Direct and indirect constraints on the W and top-quark masses. Reprinted courtesy of LEP Electroweak Working Group (Winter 2012).

where  $v \equiv \sqrt{-\mu^2/\lambda} = 246$  GeV is the *vacuum expectation value* of the scalar field  $\Phi$ . The Higgs self-interaction potential gives rise to terms involving only the physical *Higgs field* H:

$$V_H = \frac{1}{2}(2\lambda v^2)H^2 + \lambda v H^3 + \frac{\lambda}{4} H^4 \quad (3)$$

We see from Eq. (3) that the *Higgs mass*  $m_H = \sqrt{2\lambda}v$  is related to the quadrilinear self-coupling strength  $\lambda$ . It is also evident that the *trilinear self-coupling* of the Higgs field is

$$\lambda_{HHH} \equiv \lambda v = \frac{m_H^2}{2v} \quad (4)$$

and the self-coupling among four Higgs fields

$$\lambda_{HHHH} \equiv \frac{\lambda}{4} = \frac{m_H^2}{8v^2} \quad (5)$$

Note that the Higgs self-couplings are uniquely determined by the mass of the Higgs boson, which represents a free parameter of the model.

Any theoretical model based on the gauge principle must evoke spontaneous symmetry breaking. For example, the *minimal supersymmetric* extension of the Standard Model (MSSM) introduces two SU(2) doublets of complex Higgs fields, whose neutral components have vacuum expectation values  $v_1$  and  $v_2$ . In this model, spontaneous electroweak symmetry breaking results in five physical Higgs-boson states: two neutral scalar fields  $h^0$  and  $H^0$ , a pseudoscalar  $A^0$  and two charged bosons  $H^\pm$ . This extended Higgs system can be described at tree level by two parameters: the ratio  $\tan\beta \equiv v_2/v_1$ , and a mass parameter, which is generally identified with the mass of the pseudoscalar boson  $A^0$ ,  $m_A$ . While there is a bound of about 140 GeV on the mass of the lightest CP-even neutral Higgs boson  $h^0$  [4, 5], the masses of the  $H^0$ ,  $A^0$  and  $H^\pm$  bosons may be much larger. The existence of the Higgs boson  $h^0$  is the only verifiable low-energy prediction of the MSSM model.

The trilinear self-coupling of the lightest MSSM Higgs boson at tree level is given by

$$\lambda_{hhh} = \frac{m_Z^2}{2v} \cos 2\alpha \sin(\beta + \alpha) \quad \text{where} \quad \tan 2\alpha = \tan 2\beta \frac{m_A^2 + m_Z^2}{m_A^2 - m_Z^2} \quad (6)$$

We see that for arbitrary values of the MSSM input parameters  $\tan \beta$  and  $m_A$  the value of the  $h^0$  self-coupling differs from that of the SM Higgs boson. However, in the so-called ‘decoupling limit’  $m_A^2 \sim m_{H^0}^2 \sim m_{H^\pm}^2 \gg v^2/2$ , the trilinear and quadrilinear self-couplings of the lightest CP-even neutral Higgs boson  $h^0$  approach the SM value.

In contrast to any anomalous couplings of the gauge bosons, an anomalous self-coupling of the Higgs particle would contribute to electroweak observables only at two-loop and higher orders, and is therefore practically unconstrained by precision electroweak measurements [6].

### 3 Recent discovery of a Higgs-boson candidate at LHC

Preliminary results on searches for a SM Higgs boson were presented in July 2012 by the ATLAS and CMS collaborations at CERN’s Large Hadron Collider (LHC). A state decaying to several distinct final states (‘channels’) has been observed with a statistical significance of five standard deviations ( $5\sigma$ ). The evidence is strongest in the two channels with the best mass resolution: the two-photon channel (see Fig. 3) and the final state with two pairs of charged leptons (electrons or muons).

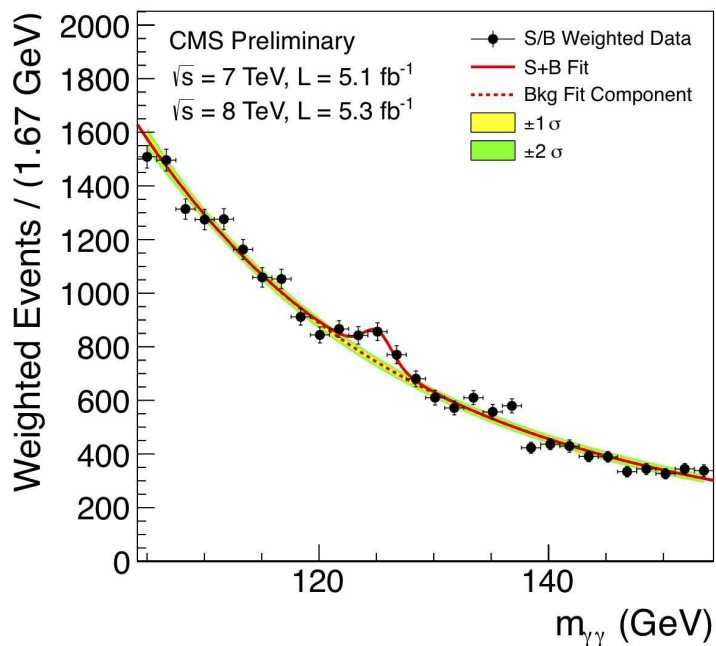


Figure 3: Di-photon ( $\gamma\gamma$ ) invariant mass distribution for the CMS data up to June 2012 (black points with error bars). The solid red line shows the fit result for signal plus background; the dashed red line shows only the background. This distribution and a similar plot by the ATLAS collaboration were first presented in July 2012.

The observed state has a mass of about 126 GeV. Its production rate is consistent, within the present statistical and systematic uncertainties, with the predicted rate for the SM Higgs boson. Event yields in different production topologies and different decay modes are self-consistent.

The CMS data rule out, at 95% confidence level (CL), the existence of the SM Higgs boson in the two broad mass ranges of 110–122.5 GeV and 127–600 GeV; the ATLAS data exclude it at 99% CL in the mass region 110–600 GeV, except in the narrow range 121.8 to 130.7 GeV. Masses up to  $\sim 115$  GeV were already excluded by CERN’s LEP collider at a similar confidence level.

## 4 Single Higgs production in $\gamma\gamma$ collisions

Since photons couple directly to all fundamental fields carrying the electromagnetic current (leptons, quarks, W bosons, supersymmetric particles),  $\gamma\gamma$  collisions provide a comprehensive means of exploring virtually every aspect of the SM and its extensions (see [7, 8] and references therein). Moreover, the cross-sections for production of charged-particle pairs in  $\gamma\gamma$  interactions are approximately an order of magnitude larger than in  $e^+e^-$  annihilations.

In  $\gamma\gamma$  collisions, the *Higgs boson* is produced as a single resonance in a state of definite CP, which is perhaps the most important advantage over  $e^+e^-$  annihilations, where this  $s$ -channel process is highly suppressed. For the Higgs mass in the range  $m_{\text{H}} = 115\text{--}200$  GeV, the effective cross-section for  $\gamma\gamma \rightarrow \text{H}$  is about a factor of five larger than that for Higgs production in  $e^+e^-$  annihilations. In this mass range, the process  $e^+e^- \rightarrow \text{HZ}$  requires considerably higher center-of-mass energies than  $\gamma\gamma \rightarrow \text{H}$ .

In  $e^+e^-$  annihilations, the heavy neutral MSSM Higgs bosons can be created only by associated production ( $e^+e^- \rightarrow H^0 A^0$ ), whereas in  $\gamma\gamma$  collisions they are produced as single resonances ( $\gamma\gamma \rightarrow H^0, A^0$ ) with masses up to 80% of the initial  $e^-e^-$  collider energy [9]. For example, if  $H^0$  and  $A^0$  have the same mass of about 500 GeV, then they could be produced either in pairs in  $e^+e^-$  annihilations at CM energies  $E_{ee} \sim 1$  TeV, or as single particles in  $\gamma\gamma$  collisions at  $E_{ee} \sim 600$  GeV.

The reaction  $\gamma\gamma \rightarrow \text{H}$ , which is related to  $\text{H} \rightarrow \gamma\gamma$ , proceeds through a ‘loop diagram’ and receives contributions from *all* charged particles that couple to the photon and the Higgs boson. Thus, the *two-photon width*  $\Gamma(\text{H} \rightarrow \gamma\gamma)$  is sensitive to the Higgs-top Yukawa coupling, as well as mass scales far beyond the energy of the  $\gamma\gamma$  collision. Assuming that the branching ratio  $\text{BR}(\text{H} \rightarrow b\bar{b})$  can be measured to an accuracy of about 2% in the process  $e^+e^- \rightarrow \text{HZ}$ , the  $\gamma\gamma$  partial width can be determined with a similar precision for  $m_{\text{H}} \simeq 120$  GeV by measuring the cross-section  $\sigma(\gamma\gamma \rightarrow \text{H} \rightarrow b\bar{b}) \propto \Gamma(\text{H} \rightarrow \gamma\gamma)\text{BR}(\text{H} \rightarrow b\bar{b})$ .

High-energy photons can be produced by Compton-backscattering of laser light on electron beams. Both the energy spectrum and polarization of the backscattered photons depend strongly on the polarizations of the incident electrons and laser photons. The key advantage of using  $e^-e^-$  beams is that they can be polarized to a high degree, enabling one to tailor the photon energy distribution to one’s needs. In a collision of two photons, the possible helicities are 0 or 2. For example, the Higgs boson is produced in the  $J_z = 0$  state, whereas the background processes  $\gamma\gamma \rightarrow b\bar{b}, c\bar{c}$  are suppressed for this helicity configuration (see Fig. 4). The circular polarization of the photon beams is therefore an important asset, for it can be used both to enhance the signal and suppress the background.

The *CP properties* of any neutral Higgs boson that may be produced at a photon collider can be *directly* determined by controlling the polarizations of Compton-scattered photons [10]. A CP-even Higgs boson couples to the combination  $\mathbf{e}_1 \cdot \mathbf{e}_2$ , whereas a CP-odd Higgs boson couples to  $(\mathbf{e}_1 \times \mathbf{e}_2) \cdot \mathbf{k}_\gamma$ :

$$\begin{aligned} \mathcal{M}(\gamma\gamma \rightarrow \text{H}[0^{++}]) &\propto \mathbf{e}_1 \cdot \mathbf{e}_2 \propto 1 + \cos 2\phi \\ \mathcal{M}(\gamma\gamma \rightarrow \text{A}[0^{-+}]) &\propto (\mathbf{e}_1 \times \mathbf{e}_2) \cdot \mathbf{k}_\gamma \propto 1 - \cos 2\phi \end{aligned}$$

where  $\mathbf{e}_i$  are polarization vectors of colliding photons,  $\phi$  is the angle between them, and  $\mathbf{k}_\gamma$  is the momentum vector of one of the Compton-scattered photons;  $0^{++}$  and  $0^{-+}$  are the quantum numbers  $\text{J}^{\text{PC}}$ . The scalar (pseudoscalar) Higgs boson couples to *linearly polarized* photons with

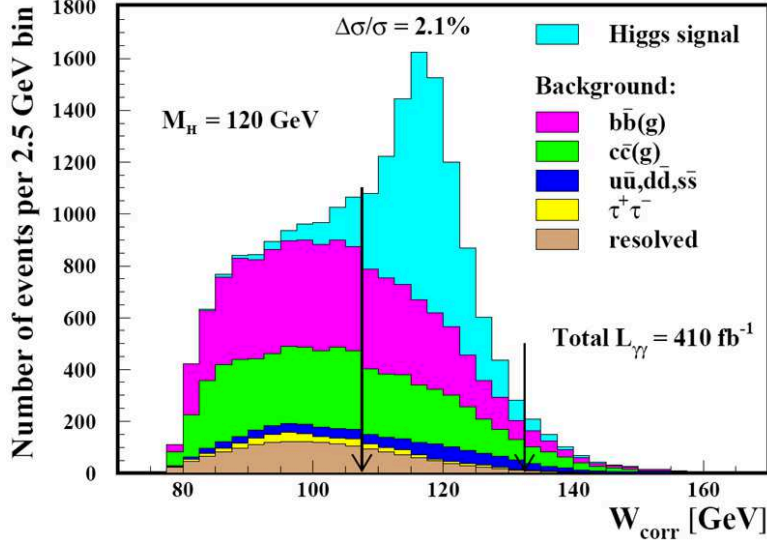


Figure 4: The reconstructed invariant-mass distribution of the  $\gamma\gamma \rightarrow H \rightarrow b\bar{b}$  signal and the  $b\bar{b}(g)$  and  $c\bar{c}(g)$  backgrounds. The gluon ('resolved') structure of the photon can be measured *in situ*. Credit: P. Niezurawski, A. Zarnecki and M. Krawczyk.

a maximum strength if the polarization vectors are parallel (perpendicular):  $\sigma \propto 1 \pm l_1 l_2 \cos 2\phi$ , where  $l_i$  are the degrees of linear polarization; the signs  $\pm$  correspond to the  $CP = \pm 1$  particles.

The general amplitude for a *CP-mixed state* to couple to two photons is

$$\mathcal{M} = \mathcal{E}(\mathbf{e}_1 \cdot \mathbf{e}_2) + \mathcal{O}(\mathbf{e}_1 \times \mathbf{e}_2)_z \quad (7)$$

where  $\mathcal{E}$  is the CP-even and  $\mathcal{O}$  the CP-odd contribution to the amplitude. If we denote the *helicities* of the two photons by  $\lambda_1$  and  $\lambda_2$ , with  $\lambda_1, \lambda_2 = \pm 1$ , then the above vector products can be expressed as

$$\mathbf{e}_1 \cdot \mathbf{e}_2 = -(1 + \lambda_1 \lambda_2)/2 \quad \text{and} \quad (\mathbf{e}_1 \times \mathbf{e}_2)_z = i\lambda_1(1 + \lambda_1 \lambda_2)/2$$

Now,

$$|\mathcal{M}_{++}|^2 - |\mathcal{M}_{--}|^2 = -4\text{Im}(\mathcal{E}\mathcal{O}^*)$$

$$2\text{Re}(\mathcal{M}_{--}^* \mathcal{M}_{++}) = 2(|\mathcal{E}|^2 - |\mathcal{O}|^2)$$

$$2\text{Im}(\mathcal{M}_{--}^* \mathcal{M}_{++}) = -4\text{Re}(\mathcal{E}\mathcal{O}^*)$$

When these expressions are divided by

$$|\mathcal{M}_{++}|^2 + |\mathcal{M}_{--}|^2 = 2(|\mathcal{E}|^2 + |\mathcal{O}|^2)$$

one obtains three *polarization asymmetries* that yield an unambiguous measure of CP-mixing [10]. It is necessary to have both *linearly* and *circularly* polarized photons in order to measure those asymmetries.

In  $e^+e^-$  annihilations, it is possible to discriminate between CP-even and CP-odd neutral Higgs bosons, but would be difficult to detect small CP-violating effects (which contribute only at the one-loop level) for a dominantly CP-even component (which contributes at the tree level in  $e^+e^-$  collisions) [11].



## 5 Single Higgs production in $e^+e^-$ annihilations

A particularly noteworthy feature of an  $e^+e^-$  collider is that the Higgs boson can be detected in the *Higgs-strahlung process*

$$e^+e^- \rightarrow \text{HZ} \tag{8}$$

even if it decays into invisible particles (e.g., the lightest *neutralino* of a supersymmetric model). In this case the signal manifests itself as a peak in the distribution of invariant mass of the system recoiling against the lepton pair stemming from Z-boson decay (see Fig. 5).

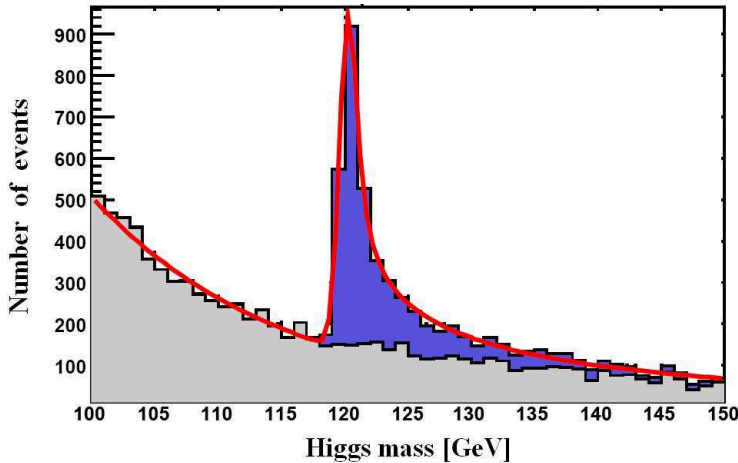


Figure 5: Distribution of the invariant mass of the system recoiling against a pair of leptons in the process  $e^+e^- \rightarrow \text{HZ} \rightarrow X\ell^+\ell^-$  for  $m_{\text{H}} = 120$  GeV and  $\int \mathcal{L} = 500 \text{ fb}^{-1}$  at  $\sqrt{s} = 250$  GeV. The red line is a fit to a Monte Carlo simulation of the Higgs signal and the ZZ background; the gray area represents the background only [12]. For  $m_{\text{H}} \simeq 120$  GeV, the optimum center-of-mass energy is  $\sqrt{s} \simeq 230$  GeV.

By exploiting the  $\text{HZ} \rightarrow X\ell^+\ell^-$  channel, the Higgs-strahlung *cross-sections* can be measured with statistical errors of 2.6 to 3.1 percent for Higgs-boson masses from 120 to 160 GeV (see [13] and references therein).

From the fits to the reconstructed mass spectra in the channels  $\text{HZ} \rightarrow q\bar{q}\ell^+\ell^-$ ,  $b\bar{b}q\bar{q}$ ,  $\text{WW}\ell^+\ell^-$  and  $\text{WW}q\bar{q}$ , the *Higgs-boson mass* can be determined with an uncertainty of 40 to 70 MeV for  $m_{\text{H}}$  in the range 120 to 180 GeV [13].

To determine the *spin* and *parity* of the SM Higgs boson in the Higgs-strahlung process, one can use the information on (1) the energy dependence of the Higgs-boson production cross-section just above the kinematic threshold, and (2) the angular distribution of the Z/H bosons. The best way to study the *CP properties* of the Higgs boson is by analyzing the spin correlation effects in the decay channel  $\text{H} \rightarrow \tau^+\tau^-$  (see [13] and references therein).

The Higgs-strahlung cross-section, which dominates at low CM energies, decreases with energy in proportion to  $1/s$  (see Eq. (20)). In contrast, the cross-section for the *W-fusion process*

$$e^+e^- \rightarrow \text{H}\nu_e\bar{\nu}_e \tag{9}$$

increases with energy in proportion to  $\log(s/m_{\text{H}}^2)$ , and hence becomes more important at energies  $\sqrt{s} \gtrsim 500$  GeV for the Higgs-mass range  $115 \text{ GeV} \lesssim m_{\text{H}} \lesssim 200 \text{ GeV}$ .

## 6 Higgs-pair production in $\gamma\gamma$ and $e^+e^-$ collisions

It is well known that hadron colliders are not ideally suited for measuring the self-coupling of the Higgs boson if  $m_{\text{H}} \leq 140$  GeV [14]. The potential of a future  $\gamma\gamma/e^+e^-$  collider for determining the HHH coupling has therefore been closely examined (see [15] and [16–20]).

The production of a pair of SM Higgs bosons in photon-photon collisions,

$$\gamma\gamma \rightarrow \text{HH} \tag{10}$$

which is related to the Higgs-boson decay into two photons, is due to W-boson and top-quark box and triangle loop diagrams. The total cross-section for  $\gamma\gamma \rightarrow \text{HH}$  in polarized photon-photon collisions, calculated at the leading one-loop order [21] as a function of the  $\gamma\gamma$  center-of-mass energy and for  $m_{\text{H}}$  between 115 and 150 GeV, is shown in Fig. 6a. The cross-section calculated for equal photon helicities,  $\sigma_{\gamma\gamma \rightarrow \text{HH}}(J_z = 0)$ , rises sharply above the  $2m_{\text{H}}$  threshold for different values of  $m_{\text{H}}$ , and has a peak value of about 0.4 fb at a  $\gamma\gamma$  center-of-mass energy of 400 GeV. In contrast, the cross-section for opposite photon helicities,  $\sigma_{\gamma\gamma \rightarrow \text{HH}}(J_z = 2)$ , rises more slowly with energy because a pair of Higgs bosons is produced in a state with orbital angular momentum of at least  $2\hbar$ .

The cross-sections for equal photon helicities are of special interest, since only the  $J_z = 0$  amplitudes contain contributions with trilinear Higgs self-coupling. By adding to the SM Higgs potential  $V(\Phi^\dagger\Phi)$  a gauge-invariant dimension-6 operator  $(\Phi^\dagger\Phi)^3$ , one introduces a gauge-invariant anomalous trilinear Higgs coupling  $\delta\kappa$  [21]. For the reaction  $\gamma\gamma \rightarrow \text{HH}$ , the only effect of such a coupling in the *unitary gauge* would be to replace the trilinear HHH coupling of the SM in Eq. 4 by an *anomalous Higgs self-coupling*

$$\lambda = (1 + \delta\kappa)\lambda_{\text{HHH}} \tag{11}$$

The dimensionless anomalous coupling  $\delta\kappa$  is normalized so that  $\delta\kappa = -1$  exactly cancels the SM HHH coupling. The cross-sections  $\sigma_{\gamma\gamma \rightarrow \text{HH}}$  for five values of  $\delta\kappa$  are shown in Fig. 6b.

In an experiment to measure the trilinear Higgs self-coupling, the contribution from  $\gamma\gamma \rightarrow \text{HH}$  for opposite photon helicities represents an irreducible background. However, this background is suppressed if one chooses a  $\gamma\gamma$  center-of-mass energy below about 320 GeV.

To ascertain the potential of  $\gamma\gamma$  colliders for measuring an anomalous trilinear Higgs self-coupling, one must take into account the fact that the photons are not monochromatic [22]. It is envisaged that an  $e^-e^-$  linac and a terawatt laser system will be used to produce Compton-scattered  $\gamma$ -ray beams for a photon collider. Both the energy spectrum and polarization of the backscattered photons depend strongly on the polarizations of the incident electrons and photons. A longitudinal electron-beam polarization of 90% and a 100% circular polarization of laser photons are assumed throughout.

The trilinear self-coupling of the Higgs boson can also be measured either in the so-called *double Higgs-strahlung process*

$$e^+e^- \rightarrow \text{HHZ} \tag{12}$$

or in the *W-fusion reaction*

$$e^+e^- \rightarrow \text{HH}\nu_e\bar{\nu}_e \tag{13}$$

The total cross-section for pair production of 120-GeV Higgs bosons in  $e^+e^-$  collisions, calculated for *unpolarized* beams, is presented in Fig. 7 for anomalous trilinear Higgs self-couplings  $\delta\kappa = 0$  or  $-1$ . If the electron beam is 100% polarized, the double Higgs-strahlung cross-section will stay approximately the same, while the W-fusion cross-section will be twice as large. From Fig. 7 we infer that the SM double Higgs-strahlung cross-section exceeds 0.1 fb at 400 GeV for  $m_{\text{H}} =$

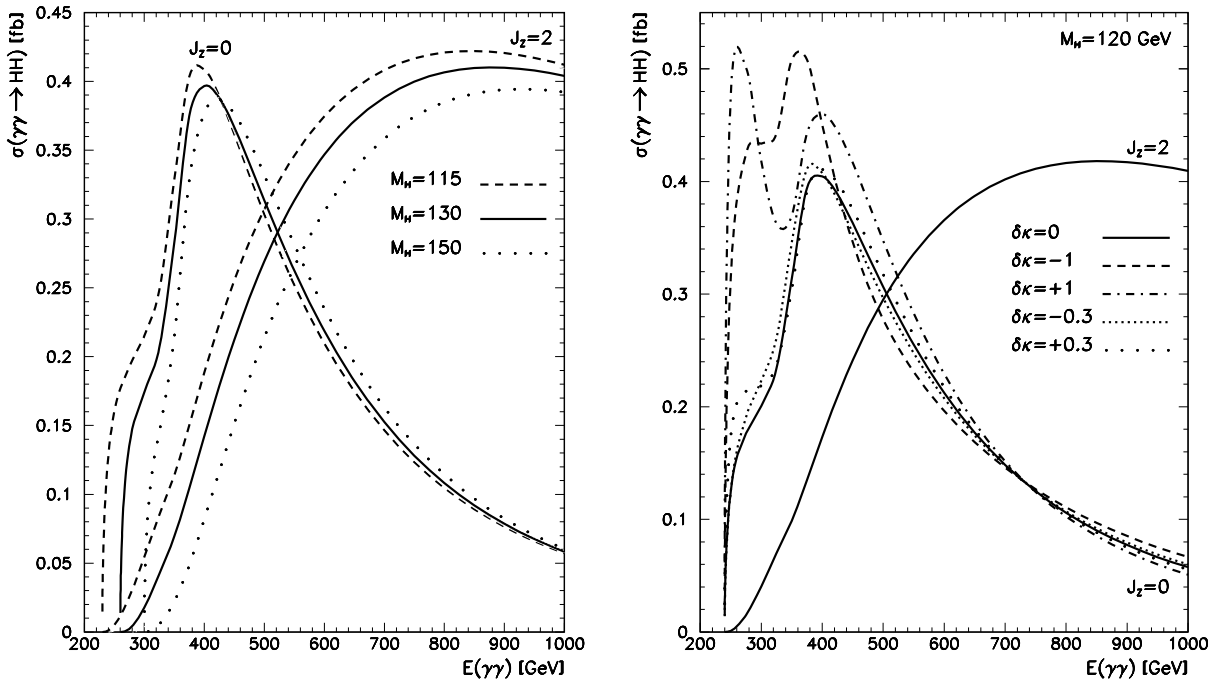


Figure 6: (a) The total  $\gamma\gamma \rightarrow HH$  cross-section as a function of the  $\gamma\gamma$  center-of-mass energy. Contributions for equal ( $J_z = 0$ ) and opposite ( $J_z = 2$ ) photon helicities are shown separately. (b) The cross-sections for HH production in  $\gamma\gamma$  collisions for  $m_H = 120$  GeV and anomalous trilinear Higgs self-couplings  $\delta\kappa = 0, \pm 1, \pm 0.3$ ; Credit: R. Belusevic and G. Jikia [15].

120 GeV, and reaches a broad maximum of about 0.2 fb at a CM energy of 550 GeV. The SM cross-section for W-fusion stays below 0.1 fb for CM energies up to 1 TeV.

For  $m_H = 120$  GeV, and assuming a longitudinal electron-beam polarization of 90%, the maximum sensitivity to an anomalous trilinear Higgs self-coupling is achieved in the double Higgsstrahlung process at a CM energy of about 500 GeV [15]. This is significantly higher than the optimal CM energy in  $\gamma\gamma$  collisions. In the W-fusion process, a similar sensitivity is attained at CM energies well above 500 GeV.

Calculations show that the *statistical* sensitivity of  $\sigma_{\gamma\gamma \rightarrow HH}$  to the Higgs self-coupling is maximal near the kinematic threshold for Higgs-pair production if  $m_H \sim 120$  GeV, and is comparable with the sensitivities of  $\sigma_{e^+e^- \rightarrow HHZ}$  and  $\sigma_{e^+e^- \rightarrow HH\nu\bar{\nu}}$  to this coupling for  $E_{ee} \leq 700$  GeV, even if the integrated luminosity in  $\gamma\gamma$  collisions is only one third of that in  $e^+e^-$  annihilations [15]. The overall *acceptance* should, in principle, be considerably larger in the process  $\gamma\gamma \rightarrow HH$  than in the reaction  $e^+e^- \rightarrow HHZ$  due to the smaller final-state particle multiplicity.

The Feynman diagrams for the process  $\gamma\gamma \rightarrow HH$  are shown in Fig. 1 of [21]. New physics beyond the Standard Model introduces additional complexity into the subtle interplay between the Higgs ‘pole amplitudes’ and the top-quark and W-boson ‘box diagrams’:

$$|\mathcal{M}(J_z = 0)|^2 = |A(s)(\lambda_{\text{SM}} + \delta\lambda) + B|^2$$

where  $\lambda_{\text{SM}}$  is the trilinear Higgs self-coupling in the SM. From the above expression we infer that the cross-section for  $\gamma\gamma \rightarrow HH$  is a quadratic function of  $\lambda \equiv \lambda_{\text{SM}} + \delta\lambda$ :

$$\sigma(\lambda) = \alpha\lambda^2 + \beta\lambda + \gamma \quad \alpha > 0, \quad \gamma > 0$$

There are various ways to define the sensitivity of the trilinear Higgs self-coupling. For instance, we can expand around  $\sigma = \sigma_{\text{SM}}$ , and express the number of events as

$$N = L\sigma_{\text{SM}} + L\delta\lambda \left( \frac{d\sigma}{d\lambda} \right)_{\lambda=\lambda_{\text{SM}}} + \dots$$

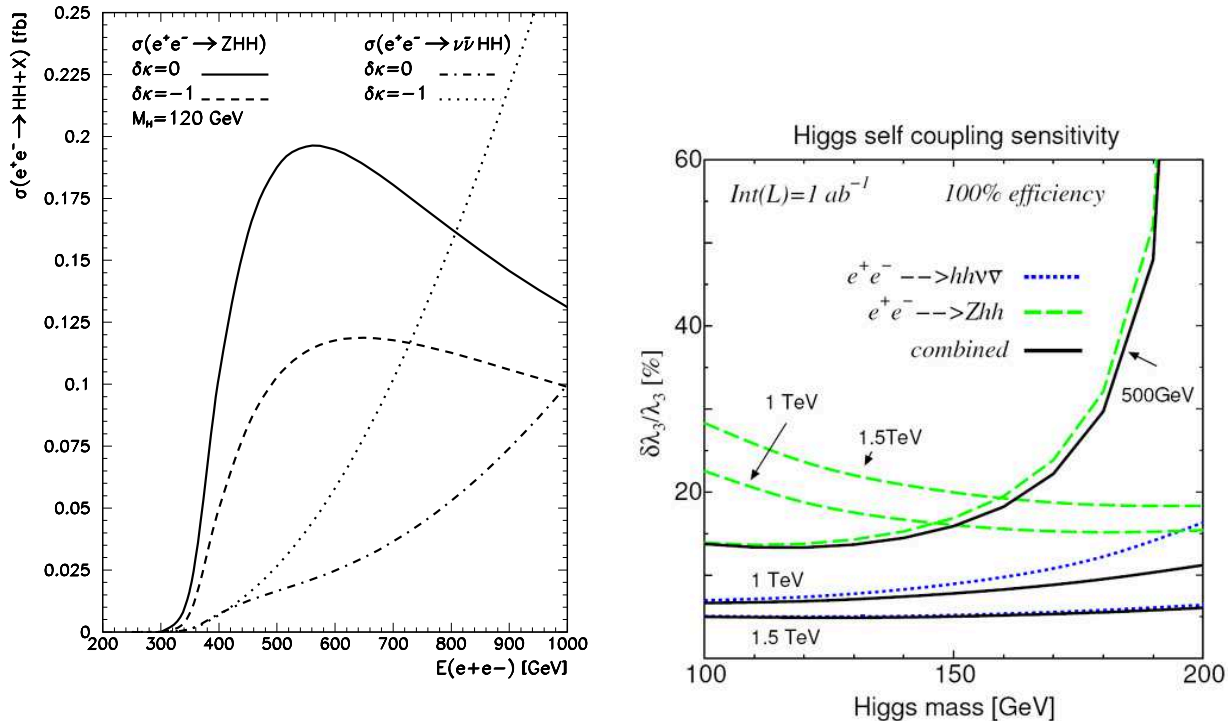


Figure 7: (a) Total cross-sections for  $e^+e^- \rightarrow \text{HHZ}$  and  $e^+e^- \rightarrow \text{HH}\nu_e\bar{\nu}_e$  as functions of the  $e^+e^-$  CM energy for  $m_H = 120$  GeV and the anomalous trilinear Higgs self-couplings  $\delta\kappa = 0$  or  $-1$  [15]. (b) Statistical sensitivity of the trilinear self-coupling for the processes  $e^+e^- \rightarrow \text{HHZ}$  and  $e^+e^- \rightarrow \text{HH}\nu_e\bar{\nu}_e$  [1].

where  $L$  is the integrated luminosity. The sensitivity of  $\lambda$  is given by

$$\sqrt{N} = \left| L \delta\lambda \left( \frac{d\sigma}{d\lambda} \right)_{\lambda=\lambda_{\text{SM}}} \right|$$

i.e.,

$$\delta\lambda = \frac{\sqrt{L \sigma_{\text{SM}}}}{L (d\sigma/d\lambda)_{\lambda=\lambda_{\text{SM}}}} = \frac{\sqrt{\sigma_{\text{SM}}/L}}{(d\sigma/d\lambda)_{\lambda=\lambda_{\text{SM}}}}$$

A plot of the trilinear Higgs self-coupling sensitivity in  $\gamma\gamma$  collisions, based on the above expression for  $\delta\lambda$ , is shown in Fig. 8; for  $e^+e^-$  annihilations, see Fig. 3.8 in [13]. An obvious drawback of the above definition of  $\delta\lambda$  is that its value becomes unphysically large when the derivative  $d\sigma/d\lambda \rightarrow 0$ , which means that one should take into account also the  $\lambda^2$  term.

Since the cross-section  $\sigma_{\gamma\gamma \rightarrow \text{HH}}$  does not exceed 0.4 fb, it is essential to attain the highest possible luminosity, rather than energy, in order to measure the trilinear Higgs self-coupling. As shown in [15], appropriate angular and invariant-mass cuts and a  $b$ -tagging requirement, which result in a Higgs-pair reconstruction efficiency of about 50%, would suppress the dominant W-pair and four-quark backgrounds well below the HH signal. For such a reconstruction efficiency, a center-of-mass energy  $E_{ee} \approx 300$  GeV and  $m_H = 120$  GeV an integrated  $\gamma\gamma$  luminosity  $L_{\gamma\gamma} \approx 450 \text{ fb}^{-1}$  would be needed to exclude a zero trilinear Higgs-boson self-coupling at the  $5\sigma$  level (statistical uncertainty only). An even higher luminosity is required for an accurate measurement of this coupling.

The results of detailed feasibility studies for measuring Higgs-pair production in  $\gamma\gamma$  and  $e^+e^-$  collisions have been reported [23, 24]. It has been shown that the optimum  $\gamma\gamma$  collision energy is around 270 GeV for a 120-GeV Higgs boson, and that the main backgrounds at this energy are

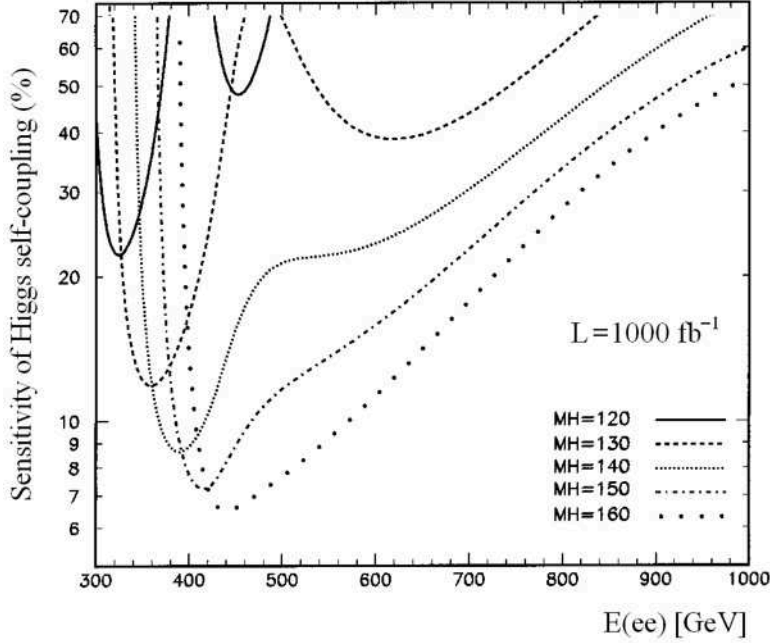


Figure 8: Statistical sensitivity of the trilinear Higgs self-coupling for various Higgs-boson masses assuming  $\int \mathcal{L} = 1000 \text{ fb}^{-1}$ . Based on the calculation by R. Belusevic and G. Jikia [15].

the processes  $\gamma\gamma \rightarrow WW, ZZ$  and  $b\bar{b}b\bar{b}$ . The preliminary analysis described in [23] suggests that  $\gamma\gamma \rightarrow HH$  could be observed with a statistical significance of  $\sim 5\sigma$  provided proper color-singlet clustering is used in jet reconstruction.

## 7 Higgs couplings to SM particles

In the *unitary gauge*, the kinetic term in Eq. (1) can be expressed as

$$(D_\mu \Phi)^\dagger (D^\mu \Phi) = \frac{1}{2} (\partial_\mu H)^2 + \frac{g^2}{4} (v + H)^2 \left( W_\mu^+ W^{-\mu} + \frac{Z_\mu Z^\mu}{2 \cos^2 \theta_W} \right) \quad (14)$$

where  $D_\mu \Phi$  is the *covariant derivative* of  $\Phi$  and

$$\cos \theta_W = \frac{g}{\sqrt{g^2 + g'^2}} \quad g \sin \theta_W = g' \cos \theta_W = e \quad (15)$$

( $g$  and  $g'$  are the electroweak couplings and  $e$  is the electric charge). A comparison with the usual mass terms for the charged and neutral vector bosons reveals that

$$m_W = \frac{gv}{2} \quad (16)$$

$$m_Z = \frac{gv}{2 \cos \theta_W} = \frac{m_W}{\cos \theta_W} \quad (17)$$

From Eq. (14) we also infer that the *Higgs-gauge boson couplings* are

$$\lambda_{HWW} \equiv \frac{g^2 v}{2} = \frac{2m_W^2}{v} \quad (18)$$

and

$$\lambda_{HZZ} \equiv \frac{g^2 v}{4 \cos^2 \theta_W} = \frac{m_Z^2}{v} \quad (19)$$

Therefore, the Higgs couplings to gauge bosons are proportional to their masses. This can be readily verified by measuring the production cross-sections in the Higgs-strahlung and W-fusion processes. At center-of-mass energies  $s \gg m_{\text{H}}^2$ ,

$$\begin{aligned}\sigma(e^+e^- \rightarrow \text{HZ}) &\propto \lambda_{\text{HZZ}}^2/s \\ \sigma(e^+e^- \rightarrow \text{H}\nu\bar{\nu}) &\propto \lambda_{\text{HWW}}^2 \log(s/m_{\text{H}}^2)\end{aligned}\tag{20}$$

The cross-section  $\sigma(e^+e^- \rightarrow \text{HZ}) \rightarrow \text{H}\ell^+\ell^-$  can be measured independently of the Higgs-boson decay modes by analyzing the invariant mass of the system recoiling against the Z boson (see Section 5).

The vector bosons are coupled to the ground-state Higgs field by means of the covariant derivative (see Eq. (14)). The *Higgs-fermion couplings* are introduced in an *ad hoc* way through the *Yukawa Lagrangian*

$$\mathcal{L} = -g_f \bar{\psi}_f \psi_f \Phi\tag{21}$$

Replacing the Higgs field by its ground-state value,  $\Phi \rightarrow v/\sqrt{2}$  (see Eq. (2)), yields the mass term  $-m_f \bar{\psi}_f \psi_f$ , where  $m_f = g_f v/\sqrt{2}$ . The interaction term in the Lagrangian is obtained by the replacement  $\Phi \rightarrow \text{H}/\sqrt{2}$ :

$$\mathcal{L}_{\text{int}} = -\frac{m_f}{v} \text{H} \bar{\psi}_f \psi_f\tag{22}$$

We see that, in the Standard Model, all the quarks and charged leptons receive their masses through *Yukawa interactions* with the Higgs field. Note also that the coupling strength between the Higgs field and the fermion  $f$  is proportional to the mass of the particle.

Using expression (16), as well as

$$m_f = \frac{g_f v}{\sqrt{2}} \quad \text{and} \quad m_{\text{H}} = \sqrt{2\lambda} v\tag{23}$$

(see Eq. (4)), we obtain<sup>1</sup>

$$v = \frac{m_{\text{W}}}{g/2} = \frac{m_{\text{H}}}{\sqrt{2\lambda}} = \frac{m_f}{g_f/\sqrt{2}}\tag{24}$$

This result is illustrated in Fig. 1 for  $m_{\text{H}} = 120$  GeV.

The Higgs-fermion couplings can be extracted by measuring the *branching fractions* of the Higgs boson (see Fig. 9). There are two methods to determine the Higgs branching fractions: (1) Measure the event rate in the Higgs-strahlung process for a given final-state configuration and then divide by the total cross-section; (2) Select a sample of unbiased events in the Higgs-strahlung recoil-mass peak and determine the fraction of events that correspond to a particular decay channel. See [13] and references therein for an estimate of the accuracy that can be achieved in such measurements.

For  $m_{\text{H}} \gtrsim 2m_{\text{W}}$ , the *total decay width* of the Higgs boson,  $\Gamma_{\text{H}}$ , is large enough to be determined directly from the reconstructed Higgs-boson mass spectrum. The result of such an analysis is shown in [13]. For smaller Higgs-boson masses,  $\Gamma_{\text{H}}$  can be determined indirectly by employing the relation between the total and partial decay widths for a given final state:

$$\Gamma_{\text{H}} = \frac{\Gamma(\text{H} \rightarrow X)}{\text{BR}(\text{H} \rightarrow X)}\tag{25}$$

---

<sup>1</sup> We can relate  $v$  to the Fermi constant  $G_{\text{F}} = 1.16639 \times 10^{-5} \text{ GeV}^{-2}$  as follows:

$$\frac{G_{\text{F}}}{\sqrt{2}} = \frac{g^2}{8m_{\text{W}}^2} = \frac{1}{2v^2} \quad \Rightarrow \quad v = (\sqrt{2}G_{\text{F}})^{-1/2} \approx 246 \text{ GeV}$$

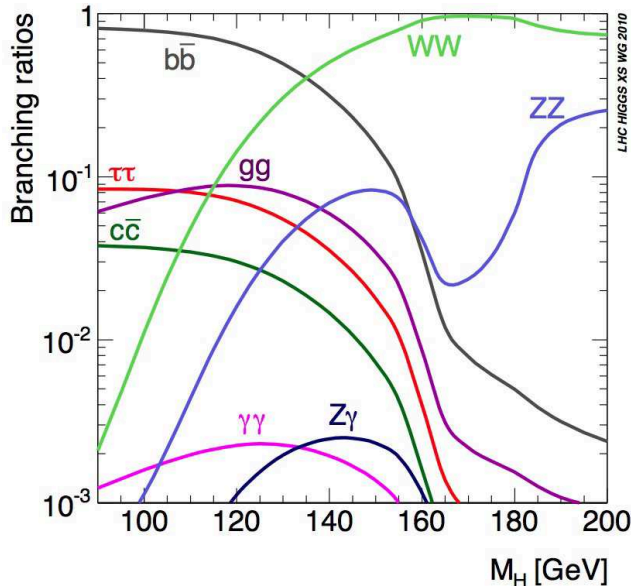


Figure 9: Decay branching fractions of the SM Higgs boson as a function of its mass. Credit: LHC Higgs XS Working Group.

For instance, consider the decay  $H \rightarrow WW^*$ . One can directly measure the branching fraction  $\text{BR}(H \rightarrow WW^*)$ , determine the coupling  $HZZ$  in the process  $e^+e^- \rightarrow HZ$ , relate the  $HZZ$  and  $HWW$  couplings based on Eqs. (18)–(19), and then use the fact that  $\Gamma(H \rightarrow WW) \propto \lambda_{HWW}^2$  to obtain the partial width  $\Gamma(H \rightarrow WW^*)$  from the information on the  $HWW$  coupling. An accuracy between 4% and 15% can be achieved in the determination of  $\Gamma_H$  for  $m_H$  up to 160 GeV [13].

The decay modes  $H \rightarrow \bar{b}b, WW$  can also be measured in photon-photon collisions with a precision similar to that expected from analyses based on  $e^+e^-$  data (see, e.g., [25]). Recall from Section 4 that the most accurate way to determine the *two-photon width*  $\Gamma(H \rightarrow \gamma\gamma)$ , which is sensitive to the Higgs-top coupling, is to combine data from  $\gamma\gamma$  and  $e^+e^-$  collisions.

## 8 The proposed facility in brief

The rich set of final states in  $e^+e^-$  and  $\gamma\gamma$  collisions at a future linear collider (LC) would play an essential role in measuring the mass, spin, parity, two-photon width and trilinear self-coupling of the Higgs boson, as well as its couplings to fermions and gauge bosons; these quantities are difficult to determine with only one initial state. Furthermore, all the measurements made at LEP and SLC could be repeated using highly polarized electron beams and at much higher luminosities. For some processes within and beyond the Standard Model (e.g., the single and double Higgs-boson production), the required center-of-mass (CM) energy is considerably lower at the facility described here than at an  $e^+e^-$  or proton collider.

A schematic layout of an X-band  $e^+e^-$  linear collider is shown in Fig. 10. Damped and bunch-compressed electron and positron beams are accelerated by a pair of linear accelerators (linacs) before colliding at an interaction point surrounded by a detector. The beams are then disposed of, and this machine cycle is repeated at a rate of 50 Hz. For a photon collider,  $\gamma\gamma$  collisions are created by Compton backscattering of FEL photons on high-energy electrons.

It is also envisaged that ‘bypass lines’ for low-energy beams would be employed to accumulate data at the Z resonance in the process  $e^+e^- \rightarrow Z$ . These runs could be used to regularly calibrate the detector, fine-tune the accelerator and measure its luminosity. Assuming a geometric lumi-

osity  $L_{e^+e^-} \approx 5 \times 10^{33} \text{ cm}^{-2} \text{ s}^{-1}$  at the Z resonance, approximately  $2 \times 10^9$  Z bosons could be produced in an operational year of  $10^7$  s; this is about 200 times the entire LEP statistics.

The proposed facility would be constructed in several stages, each with distinct physics objectives that require particular center-of-mass (CM) energies. The processes to be studied, and the corresponding CM energies, are [20]:

- $e^+e^- \rightarrow Z, WW; \quad \gamma\gamma \rightarrow H$        $E_{ee} \sim 90 \text{ to } 170 \text{ GeV}$
- $e^+e^- \rightarrow ZH$        $E_{ee} \sim 250 \text{ GeV}$
- $\gamma\gamma \rightarrow HH; \quad e^+e^- \rightarrow t\bar{t}$        $E_{ee} \sim 330 \text{ to } 350 \text{ GeV}$

The top-quark mass and the Higgs-top coupling could be measured in the process  $e^+e^- \rightarrow t\bar{t}$  at the pair-production threshold [26]; one expects  $\delta m_t \approx 100 \text{ MeV} \approx 0.1\delta m_t(\text{LHC})$ .

The production and testing of the accelerating structures and rf sources needed for an energy upgrade, and the subsequent installation of the rf sources, can be carried out with minimal disruption to the data-taking process if the klystrons, modulators and pulse compressors are placed in a separate tunnel (see Fig. 11).

There are several notable differences between this and other designs based on the X-band technology (NLC/JLC, GLC [1] and CLICHE [25]): (1) The proposed facility would utilize high-gradient CLIC-type cavities and a klystron-based power source; a two-beam scheme could be implemented at a later stage. (2) There would be only one interaction region and a single beam dumping system for both  $e^+e^-$  and  $\gamma\gamma$  beams. (3) In its first stage of operation ( $E_{ee} \sim 170 \text{ GeV}$ ), the entire facility could be placed *within* a site only 3 km long. A facility with these characteristics was originally proposed in [20] (see also [27]).

## 9 The X-band accelerator complex

A schematic layout of an X-band linear  $e^+e^-$  collider is shown in Fig. 10. The 11.4 GHz X-band rf technology was originally developed at SLAC and KEK [28]. The choice of this technology is motivated by the cost benefits of having relatively low rf energy per pulse and high accelerating gradients. The ongoing effort to develop high-gradient X-band structures is essential for the eventual construction of a CLIC-type linear accelerator [29].

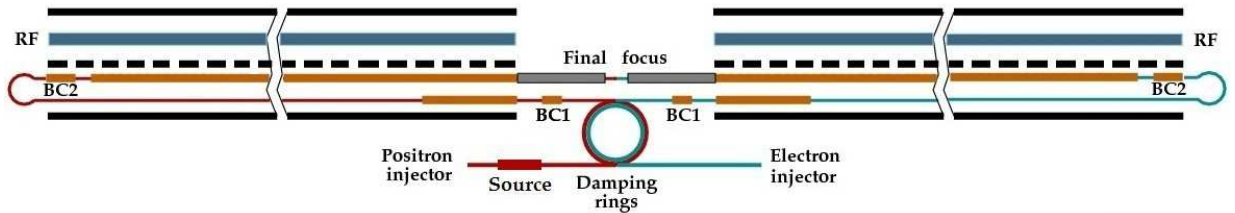


Figure 10: Schematic layout of an X-band linear  $e^+e^-$  collider. With a crossing angle at the interaction point (IP), separate beam lines can be used to bring the disrupted beams to their respective dumps, thereby enabling post-IP diagnostics. A two-stage bunch compression system (BC) is envisaged.

The tunnels containing the rf sources and accelerating structures are sketched in Fig. 11. As mentioned in Section 8, damped and bunch-compressed electron and positron beams are accelerated by a pair of linacs before colliding at the interaction point. The beams are then disposed of, and this machine cycle is repeated at a rate of 50 Hz. ‘Bypass lines’ for low-energy beams would be employed. Rough design parameters of the machine are shown in Fig. 12 (see [1, 30]).



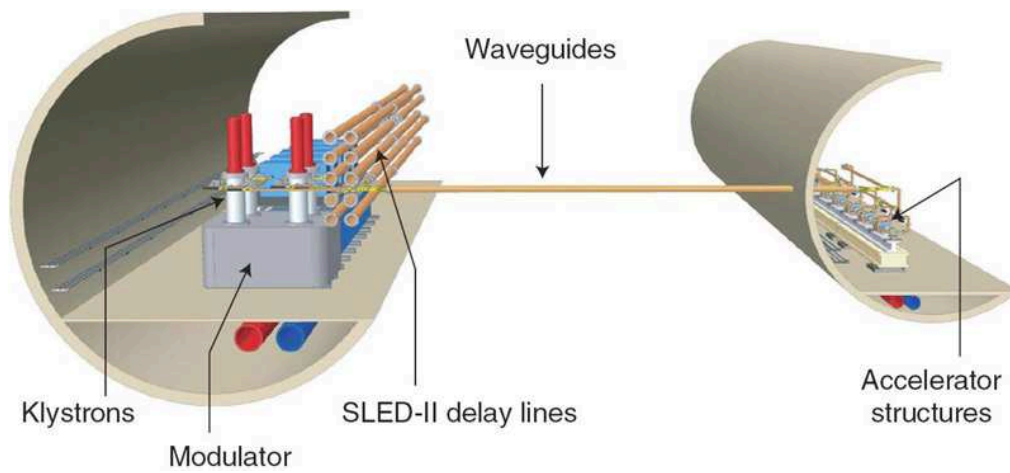


Figure 11: Dual tunnels for an X-band linear collider [1].

A comprehensive review of the status of X-band accelerator technology is given in [28]. Since then, significant advances have been made in pulsed HV and rf power generation, high gradient acceleration and wakefield suppression. The ultimate design of rf cavities will depend on the outcome of the ongoing effort to develop 100 MeV/m X-band structures for a CLIC-type linear collider (see Section 10).

	GLC	CLIC500	CLIC	Stage 2
Total CM energy (GeV)	500	500	3000	<b>250</b>
Loaded accelerator gradient (MV/m)	50	80	100	<b>85</b>
Effective gradient (MV/m)	44			<b>70</b>
Linac length (km)	14.5			<b>3.6</b>
Klystron peak power (MW)	75			<b>50</b>
Klystron pulse length ( $\mu\text{s}$ )	1.6			<b>1.6</b>
Pulse compression ratio	4			<b>6</b>
Power / structure (MW)	75			<b>46</b>
RF pulse length (ns)	400			<b>245</b>
Beam current (A)	0.86	2.2	1.2	<b>1.13</b>
Number of particles in a bunch ( $10^{10}$ )	0.75	0.68	0.37	<b>0.37</b>
Bunch spacing (ns)	1.4	0.5	0.5	<b>0.52</b>
Number of bunches / train	192	354	312	<b>312</b>
Bunch train length (ns)	267	177	156	<b>163</b>

Figure 12: Rough design parameters of the machine.

## 10 The RF system

A single rf unit contains a modulator that drives a pair of 50 MW klystrons, each of which generates 1.6  $\mu\text{s}$  rf pulses at 50 Hz (see Figs. 13 and 14). An rf compression system enhances the peak power of the klystrons by a factor of 3.75, and produces 245 ns pulses that match the accelerator structure requirements.<sup>2</sup> The resulting 375 MW, 245 ns pulses feed seven 0.21m-long accelerator structures, producing a 85 (100) MV/m loaded (unloaded) gradient in each structure.

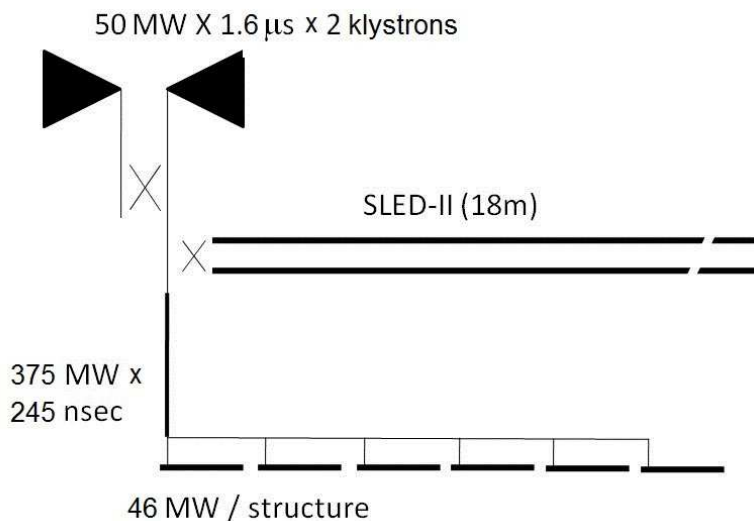


Figure 13: Schematic of the RF acceleration system.

	GLC	CLIC500	CLIC	Present
Modulator				<b>Solid-state</b>
Klystron				<b>XL4</b>
Pulse compression				<b>SLED II</b>
Power delivery				<b>Low loss WG</b>
Acc. structure length (m)	0.6		0.25	<b>0.21</b>
Phase advance / cell	$5\pi/6$	$5\pi/6$	$2\pi/3$	<b><math>2\pi/3</math></b>
Structure filling time (ns)	120	50	67	<b>59</b>
Beam hole aperture ( $a/\lambda$ )	0.21-0.15	<0.145>	<0.11>	<b>&lt;0.11&gt;</b>
Vg/c (%)	5.1 – 1.1	1.9 – 1.1	1.7 – 0.8	<b>1.7 - 0.8</b>

Figure 14: Rough design parameters of the RF system.

<sup>2</sup> It takes 59.4 ns (filling time) plus 22.4 ns (ramping time) to fill each rf cavity with an accelerating field. The remaining period of 163 ns is used to accelerate a ‘train’ of electron bunches.

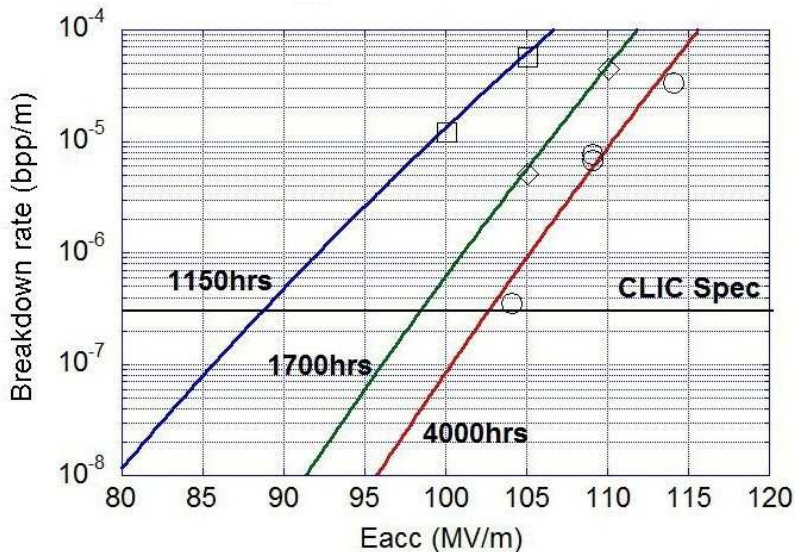


Figure 15: Breakdown rate of the CLIC prototype rf cavity TD24#4 [31].

The latest test results for one of the CLIC prototype rf cavities TD24 are presented in Fig. 15. The cavity reached the indicated CLIC breakdown rate requirement in less than 2000 hours. Based on these results, we have chosen a value of 85 MeV/m for the beam-loaded accelerator gradient.

To reduce power consumption, it was proposed [32] to use klystrons with superconducting solenoidal focusing. The XL4 klystron developed at SLAC, for instance, could initially be adapted for this purpose. Alternatively, one could employ klystrons with periodic permanent magnet (PPM) focusing [33]. However, all PPM klystrons built so far suffer chronic rf breakdown in the output section, which manifests itself by a loss of transmitted power that develops over several hundred ns [28].

For cost reasons, it is preferable to power as many klystrons per pulse modulator as possible. With this in mind, a solid-state induction-type modulator that could drive a pair of 50 MW X-band klystrons was designed at SLAC [28]. Another possible choice are solid-state modulators produced by ScandiNova.

## 11 Photon collider

The idea of using counter-directed electron linacs to create a gamma-gamma collider can be traced back to an article by P. Csonka<sup>3</sup> published in 1967 [34]. The seminal work on photon colliders by I. Ginzburg et al. [35] describes in detail a method for obtaining  $\gamma\gamma$  and  $e\gamma$  collisions by Compton backscattering of laser light on high-energy electrons.

The backscattered photons have energies comparable to those of the incident electrons (see Fig. 16), and follow their direction with some small angular spread of the order of  $1/\gamma$ , where  $\gamma$  is the Lorentz factor. The spatial spread of the photons is approximately  $d/\gamma$  at a distance  $d$  from the Compton interaction point (CIP). Both the energy spectrum and polarization of the backscattered photons depend strongly on the polarizations of the incident electrons and laser photons. The key advantage of using  $e^-e^-$  beams at a  $\gamma\gamma$  collider is that they can be polarized to a high degree.

At CIP, the electron beam is about 10 times wider than it would be at the  $ee$  collision point

<sup>3</sup>One of the present authors (R. Belusevic) has maintained a keen interest in Paul Csonka's pioneering idea since the late 1970s.

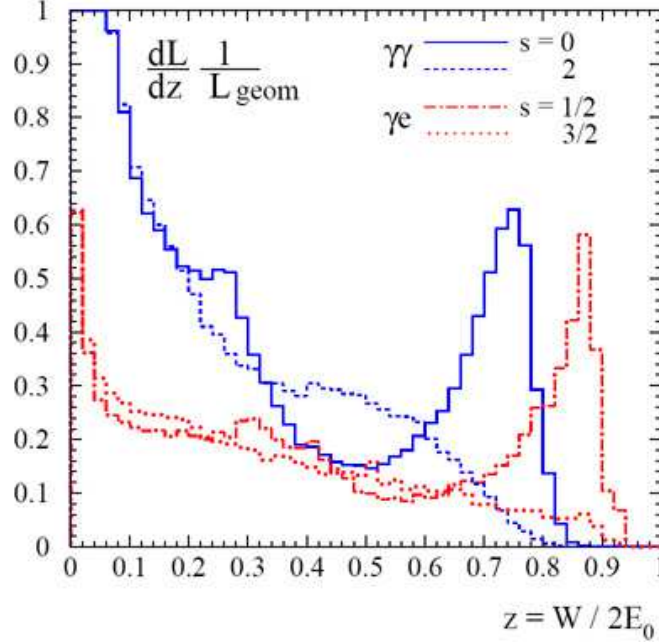


Figure 16: Simulated  $\gamma\gamma$  and  $e\gamma$  luminosity spectra [36].

in the absence of a laser beam. However, since the backscattered photons follow the direction of the incident electrons, they are automatically ‘focused’ to their collision point.

The absence of beam-beam effects in  $\gamma\gamma$  collisions means that it is not necessary to have very flat linac beams. The spectral luminosity of  $\gamma\gamma$  collisions strongly depends on beam characteristics, but only through the parameter  $\rho$ , the ratio of the intrinsic transverse spread of the photon beam to that of the original electron beam:  $\rho \equiv d/\gamma\sigma_e$ . In this expression,  $d$  is the distance between CIP and the photon-photon collision point,  $\gamma$  is the Lorentz factor and  $\sigma_e$  is the radius that a round Gaussian linac beam would have at the collision point in the absence of a laser beam. As  $\rho$  increases, the the monochromaticity of the luminosity distribution improves (because the lowest-energy photons, which scatter at the largest angles, do not pass through the collision point), but the total luminosity decreases. For a typical photon collider, the optimal value of  $d$  is a few millimeters [37].

Assuming that the mean number of Compton interactions of an electron in a laser pulse (the Compton conversion probability) is 1, the *conversion coefficient*  $k \equiv n_\gamma/n \approx 1 - e^{-1} = 0.63$ , where  $n_e$  is the number of electrons in a ‘bunch’ and  $n_\gamma$  is the number of scattered photons. The luminosity of a gamma-gamma collider is then

$$\mathcal{L}_{\gamma\gamma} = (n_\gamma/n_e)^2 \mathcal{L}_{ee} \approx (0.63)^2 \mathcal{L}_{ee} \quad (26)$$

where  $\mathcal{L}_{ee}$  is the *geometric luminosity* of electron beams:

$$\mathcal{L}_{ee} = \frac{\gamma n_e^2 N_b f}{4\pi \sqrt{\varepsilon_x \beta_x \varepsilon_y \beta_y}} \quad (27)$$

In this expression,  $\varepsilon_x, \varepsilon_y$  are the *beam emittances*,  $\beta_x, \beta_y$  are the horizontal and vertical *beta functions*, respectively,  $N_b$  is the number of bunches per train, and  $f$  is the beam collision frequency. In the high-energy part of the photon spectrum,  $\mathcal{L}_{\gamma\gamma} \sim 0.1\mathcal{L}_{ee}$ . However, if beams with smallest possible emittances and stronger beam focusing in the horizontal plane are used, then  $\mathcal{L}_{\gamma\gamma}$  could, in principle, exceed  $\mathcal{L}_{e^+e^-}$  [36] (see also Section 14).

## 12 Laser system for an X-band machine

In order to attain maximum luminosity, every electron bunch in the accelerator should collide with a laser pulse of sufficient intensity for 63% of the electrons to undergo a Compton scattering. This requires a laser system with high average power, capable of producing pulses that would match the temporal spacing of electron bunches. The laser power is minimized when the Rayleigh range of the laser focus and the laser pulse width are matched to the electron bunch length. The proposed collider would have about 300 50-micron bunches separated by 0.5 ns, with 50 trains per second. This means that  $300 \times 50 = 15000$  laser pulses with a duration of approximately 1 ps must be produced every second. To avoid nonlinear electrodynamic effects, the maximum pulse energy should not exceed a couple of joule. Therefore, the laser system ought to deliver at least 15 kW of average power in pulses of a terawatt peak power, matched to the linac bunch structure.

These requirements could be satisfied by an optical *free electron laser* (FEL). The radiation produced by an FEL has a variable wavelength, and is fully polarized either circularly or linearly depending on whether the undulator is helical or planar, respectively. The required time structure of laser pulses can be achieved by using an S-band linac for the FEL. A free electron laser for a photon collider is described in [38].

The wavelength  $\lambda$  of FEL radiation is determined by  $\lambda \approx \lambda_u/2\gamma^2$ , where  $\gamma$  is the Lorentz factor of the electron beam and  $\lambda_u$  is the periodic length of the undulator. An optical FEL requires a much smaller electron linac and a considerably simpler undulator than an XFEL. However, the charge per electron beam bunch has to be sufficiently large ( $\sim 5$  nC) to produce photon pulses of  $\sim 1$  J. Suitable high-intensity and low-emittance rf guns have already been developed [39]. An optical FEL could be placed in a separate tunnel connected to the experimental hall housing the detector.

## 13 Interaction region and beam dump

The location of beamline elements near the interaction region (IR) of an  $e^+e^-$  collider and their integration with a generic detector are discussed at length in [30] and [40].

The *assembly* for the interaction region at a photon collider shown in Fig.17 satisfies the following requirements: (a) the laser beam must be nearly co-linear with the electron beam; (b) the latter must pass through the final focusing optics; (c) the beams of electrons and laser photons must simultaneously be at the Compton interaction point; (d) the duration of the laser pulse must correspond to the electron bunch length.

The Compton scattering of laser photons on high-energy electrons results in a large energy spread in the electron beam. At the interaction point (IP), this leads to a large angular spread of the outgoing beam due to the beam-beam interaction. For nominal beam and laser parameters, the extraction beam pipe must therefore have an aperture of about  $\pm 10$  milliradians.

To remove the disrupted beams, one can use the *crab-crossing scheme* proposed by R. Palmer. In this scheme, the beams are collided at a *crossing angle* of about 10 to 20 milliradians. The same luminosity as in head-on collisions can be obtained by tilting the electron bunches with respect to the direction of the beam motion.

The aperture of the extraction beam pipe and the physical size of the final focusing magnet set a lower limit on the crossing angle of the colliding beams. The minimum crossing angle is about 25 milliradians if a final focusing quadrupole magnet with a compensating coil to minimize the fringe field is used [43].<sup>4</sup> This is somewhat larger than the crossing angles envisaged for the proposed GLC and NLC X-band  $e^+e^-$  colliders.

---

<sup>4</sup> The fringe field from the final focusing magnet must be minimized to prevent low-energy particles, which are swept away by the field, from causing radiation- and heat-related problems.

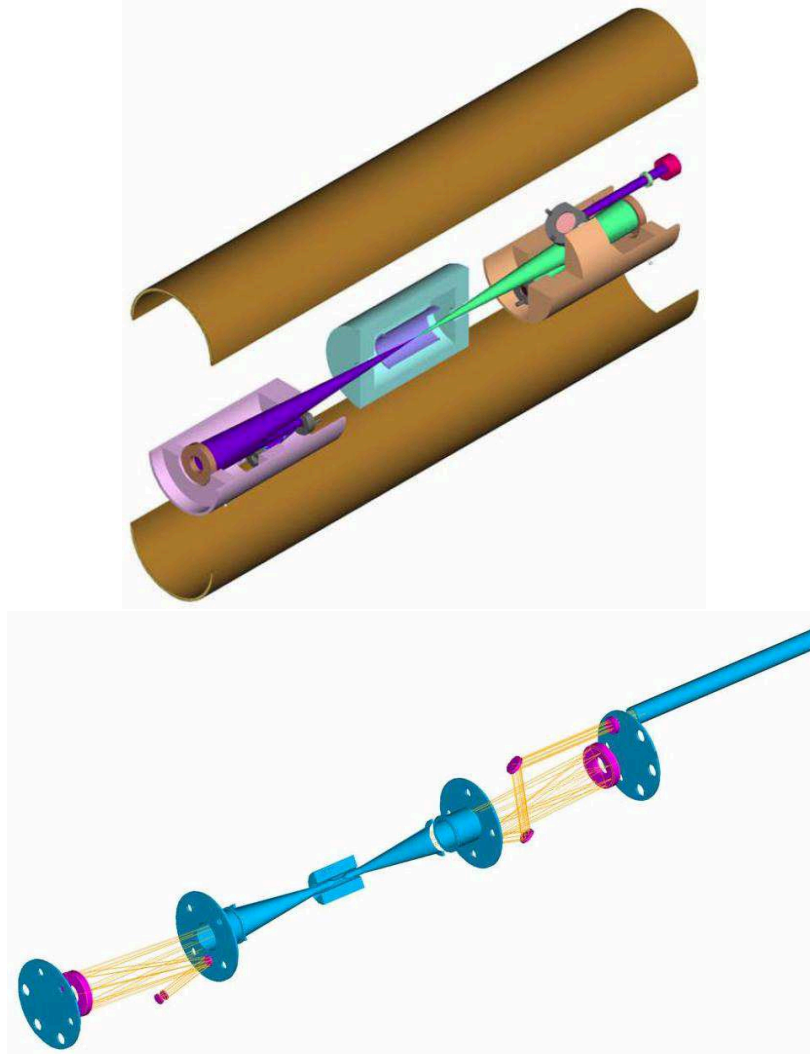


Figure 17: Optics assembly at the  $\gamma\gamma$  interaction region. Electron beams and most of the background particles pass through the central hole in each of the two end-mirrors. Elements of the assembly were designed, simulated and prototyped at LLNL [41, 42].

The ‘feedback’ system for bringing the beams into collision relies on post-IP *beam position monitors* (BPMs) that measure the beam-beam deflection at the collision point. Because of the energy spread in a highly disrupted beam, conventional BPMs may not provide sufficient resolution due to electric noise. Moreover, it is not possible to steer such a beam without large beam losses. This implies that the extraction line at a  $\gamma\gamma$  collider will be a straight vacuum pipe, which precludes some post-IP diagnostics such as precise measurement of the beam energy and polarization.

Much of the extracted-beam power will be in the form of high-energy photons that have a very narrow angular spread. This would result in a large amount of energy being deposited within a small volume of the water *beam dump*, causing vaporization of  $\text{H}_2\text{O}$ . A possible solution to this problem would be to convert the photons to  $e^+e^-$  pairs in a gas target situated before the dump. In order to decrease the flux of backward-scattered neutrons, a volume filled with hydrogen or helium gas could be placed just before the gas target (see [44] and [36] for more detail).

Huge savings in construction cost could be achieved if the crossing angle and the beam dump are exactly the same for the operation of the accelerator in the  $e^+e^-$  and  $\gamma\gamma$  collision modes. The beam dump described in [44] is designed with this in mind. The part of the extraction line

containing a chicane — which provides vertical displacement and dispersion needed for continuous measurements of the beam energy spectrum and polarization at an  $e^+e^-$  collider — could be replaced with a straight vacuum pipe for the operation in the  $\gamma\gamma$  mode.

## 14 Luminosity and backgrounds at a $\gamma\gamma$ collider

Since the cross-sections  $\sigma_{\gamma\gamma \rightarrow \text{HH}}$  and  $\sigma_{e^+e^- \rightarrow \text{HHZ}}$  do not exceed 0.4 fb, it is essential to attain the highest possible luminosity, rather than energy, in order to measure the trilinear Higgs self-coupling. If beams with smallest possible emittances and stronger beam focusing in the horizontal plane are used, then the  $\gamma\gamma$  luminosity  $\mathcal{L}_{\gamma\gamma}$  could, in principle, be made higher than  $\mathcal{L}_{e^+e^-}$ , as explained in what follows [36].

At a photon collider with CM energies  $\lesssim 500$  GeV, and for electron beams that are not too short, coherent pair production is suppressed due to the broadening and displacement of the electron beams during their collision. In this case,  $\mathcal{L}_{\gamma\gamma}$  is limited *only* by the transverse area of the beam (note that its vertical size is much smaller than the horizontal):

$$\mathcal{L}_{\gamma\gamma} \propto (\sigma_x \sigma_y)^{-1} \quad \sigma_{x,y} = \sqrt{\beta_{x,y}(\varepsilon_{x,y}/\gamma)} \quad (28)$$

as can be seen from expressions (26) and (27) in Section 11.

The beam emittances in Eq. (28) are determined by various physics effects inside a damping ring (see Fig. 18). If the synchrotron radiation is dominated by the ring's wiggler parameters (large  $F_w$ ), and if the quantum excitation by the wiggler is not too large compared with that in the arcs, then from Eqs. (33) and (14) in [45] it follows that the horizontal beam emittance  $\varepsilon_x$  could be significantly reduced by using a wiggler with short period and a judiciously chosen value of the peak field (in order to preserve the damping time). The vertical emittance  $\varepsilon_y$  is *not* determined by the wiggler, but by optics errors that are not easily characterized. Assuming, for instance, that  $\varepsilon_x$  could be reduced by a factor of 6 and  $\varepsilon_y$  by a factor of 4 compared with their 'nominal' ILC values,  $\mathcal{L}_{\gamma\gamma}$  would then exceed  $\mathcal{L}_{e^+e^-}$ :

$$\mathcal{L}_{\gamma\gamma}(\text{high-energy peak}) \sim 1.2 \mathcal{L}_{e^+e^-}$$

where  $\mathcal{L}_{e^+e^-} \approx 2 \times 10^{34} \text{ cm}^{-2} \text{ s}^{-1}$  is limited by collision effects (beamstrahlung and beam instabilities) [36]. To obtain this result it was also assumed that  $\beta_x = 1.7$  mm and that the distance between the interaction and conversion  $d = 1$  mm. Note that the minimum value of  $\beta_x$  is restricted by chromo-geometric aberrations in the final-focus system. Simulated luminosity spectra for these values of  $\beta_x$  and  $d$  are shown in Fig. 16.

At a  $\gamma\gamma$  collider, the spectrum of photons after Compton scattering is broad, with a characteristic peak at maximum energies (see Fig. 16). The low-energy part of the spectrum is produced by multiple Compton scattering of electrons on photons inside laser beams.

The Compton-scattered photons can have circular or linear polarizations, depending on their energies and the polarizations of the initial electrons and laser light. For instance, the scattered photons have an average helicity  $\langle \lambda_\gamma \rangle \neq 0$  if either the laser light has a circular polarization  $P_c \neq 0$  or the incident electrons have a mean helicity  $\langle \lambda_e \rangle \neq 0$ . In the case  $2P_c \lambda_e = -1$ , which results in a good monochromaticity of the backscattered photon beam, the average degree of circular polarization of the photons within the high-energy peak of the luminosity distribution is over 90%.

Since the polarization of Compton-scattered photons depends strongly on their energy, the *luminosity spectrum* has to be measured separately for different polarization states. When both photons are *circularly polarized*, the process  $\gamma\gamma \rightarrow e^+e^-, \mu^+\mu^-$  is particularly well suited for measuring the spectral luminosity [46]. This process has a cross-section of a few pb for a total  $\gamma\gamma$  angular momentum  $|J_z| = 2$ . A precision of about 0.1% is expected in one year of running, which is better than the accuracy needed for the Higgs-boson studies described in this note. To measure



Figure 18: Arc section of the ATF Damping Ring, which produces the world’s smallest-emittance beams. The layout of the magnets in the arc sections is designed to achieve small equilibrium emittances. The wiggler magnets in the straight sections of the ring shorten the damping time. Fast kicker magnets and DC septum magnets are used for beam extraction. Credit: ATF team.

the luminosity spectrum in the  $|J_z| = 0$  configuration, the helicity of one of the photon beams can be inverted by simultaneously changing the signs of the helicities of both the laser and electron beams. For the product of photon *linear polarizations*, the spectral luminosity can be measured in the above process by studying the azimuthal variation of the cross-section at large angles [46, 37].

Undisrupted electron beams at a  $\gamma\gamma$  collider can be steered using a fast feedback system that measures their deflection (see Section 13). Once the electron beams are brought into collision, the laser will be turned on. The scattered photons follow the direction of the incident electrons.

Multiple Compton scattering of electrons on photons leads to a low-energy ‘tail’ in the energy spectrum of the electrons. At the interaction point, this results in a large deflection angle of the  $e^-e^-$  beams. Due to a finite crossing angle (see Section 13), the outgoing beams are also deflected vertically by the solenoidal magnetic field of the detector. Fig. 19 in [47] shows the angular spread of an outgoing electron beam right after the interaction point and at  $z = 2.8$  m. The problem of ‘stabilizing’ beam-beam collisions, and hence the  $\gamma\gamma$  luminosity, is discussed in [36].

The *backgrounds* at a photon collider caused by beam-beam effects in the interaction region have been simulated considering both the *incoherent* particle-particle and *coherent* particle-beam electromagnetic interactions [37]. Another significant source of background is due to backscattering of particles. The hadronic structure of the photon arises from the possibility that it can either split into a quark-antiquark pair or transform into a vector meson, with the probability of about 1/200. At the expected ILC  $\gamma\gamma$  luminosity, for instance, the average number of hadronic background events per one bunch collision is about two [37]. The above backgrounds influence data acquisition and analysis, as well as the operation of various detector components [37, 47].



## 15 Main advantages over a TESLA-type design

A detailed description of the *International Linear Collider* (ILC) design can be found in [40]. This design, based on the superconducting technology originally developed at DESY, uses L-band (1.3 GHz) rf cavities that have average accelerating gradients of  $\sim 31.5$  MeV/m. A single superconducting niobium cavity is about 1 m long. Nine cavities are mounted together in a string and assembled into a common low-temperature cryostat or *cryomodule*, which is 12.652 m long.

The ILC main linacs are composed of rf units, each of which is formed by three contiguous cryomodules containing 26 nine-cell cavities. Every unit has an rf source, which includes a pulse modulator, a 10 MW multi-beam klystron, and a waveguide system that distributes the power to the cavities.

This L-band (TESLA-type) design offers some advantages over the X-band technology:

- Wakefields are considerably reduced due to the large size of the rf cavities, which means that cavity alignment tolerances<sup>5</sup> can be relaxed;
- Superconducting rf cavities can be loaded using a long rf pulse (1.5 ms) from a source with relatively low peak rf power;
- ‘Wall-plug to beam’ power transfer efficiency is considerably higher than for a klystron-based X-band machine;
- The long rf pulse allows a long bunch train ( $\sim 1$  ms), with many bunches ( $\sim 2600$ ) and a relatively large bunch spacing ( $\sim 370$  ns). A trajectory correction (feedback) system within the train can therefore be used to bring the beams into collision.

However, in contrast to a compact, high-gradient X-band machine, a collider based on the current TESLA-type design would be characterized by low accelerating gradients, damping rings whose length (at least 6 kilometers) limits the luminosity of the machine, and a technologically challenging cryogenic system comprising a number of surface cryogenic plants. Such plants require access roads and an electric power-supply network, and have to be connected to the accelerator via horizontal or vertical shafts.

Low-gradient, TESLA-type linacs are bound to be very long. A considerable fraction of the total cost of the accelerator would therefore be spent on civil engineering, whereas for an X-band machine it would be spent mainly on the accelerating structures and rf sources. But the most serious drawback, in our opinion, of the TESLA-type design is that it cannot be used as a prototype for a high-gradient, TeV-scale linear collider such as CLIC.

It is also important to bear in mind that the electron bunches in a TESLA-type machine are considerably longer than in an X-band linac, which means that more powerful laser pulses are needed to achieve comparable photon densities at the Compton interaction region.

## 16 Summary and Acknowledgements

The rich set of final states in  $e^+e^-$  and  $\gamma\gamma$  collisions at a future linear collider would play an essential role in measuring the mass, spin, parity, two-photon width and trilinear self-coupling of the Higgs boson, as well as its couplings to fermions and gauge bosons (see Sections 4 to 6); these quantities are more difficult to determine with only one initial state. For some processes within and beyond the Standard Model, the required center-of-mass energy is considerably lower at the facility described here than at an  $e^+e^-$  or proton collider.

Since the cross-sections  $\sigma_{\gamma\gamma \rightarrow \text{HH}}$  and  $\sigma_{e^+e^- \rightarrow \text{HHZ}}$  do not exceed 0.4 fb, it is essential to attain the highest possible luminosity, rather than energy, in order to measure the trilinear Higgs self-

---

<sup>5</sup>In the main linac of a linear collider, the principal sources of emittance growth are misaligned quadrupoles (which introduce dispersion) and off-axis accelerating cavities (which generate transverse wakefields).

coupling. If beams with smallest possible emittances and stronger beam focusing in the horizontal plane are used, then the luminosity  $\mathcal{L}_{\gamma\gamma}$  could, in principle, exceed  $\mathcal{L}_{e^+e^-}$  (see Section 14).

The proposed  $e^+e^-/\gamma\gamma$  collider would be constructed in several stages, each with a distinct physics objective that requires a particular center-of-mass energy (see Section 8 and the preprint in [15]). Together with LHC, such a facility would bridge the gap between the present high-energy frontier and that accessible to a TeV-scale  $e^+e^-$  or muon collider. Moreover, the proposed facility would also serve as a prototype for a linear collider with high accelerating gradients based on the CLIC design.

If the initial operation of the proposed facility is in the  $\gamma\gamma$  mode, there would be no need for an  $e^+$  source. Two electron damping rings could then be built inside a single tunnel. For operation at the nominal  $e^+e^-$  luminosity, a positron damping ring would later replace one of the electron rings.

A possible source of primary photons for a  $\gamma\gamma$  collider is an optical *free electron laser* (FEL). The radiation produced by an FEL has a variable wavelength and is fully polarized either circularly or linearly. Each of the three currently operating X-ray free electron lasers (XFELs) — at SLAC (S-band), DESY (L-band) and the SPring-8 facility (C-band) — can serve as a testbed for an optical FEL.

Elements of the optics assembly for the interaction region at a photon collider were designed, simulated and prototyped at LLNL (see Section 13). The Compton scattering of laser photons on high-energy electrons results in a large energy spread in the electron beam. At the interaction point, this leads to a large angular spread of the outgoing beam due to the beam-beam interaction. To remove the disrupted beams, one can use the crab-crossing scheme described in Section 13. Huge savings in construction cost could be achieved if the crossing angle and the beam dump are exactly the same for the operation of the accelerator in the  $e^+e^-$  and  $\gamma\gamma$  collision modes.

An L-band (TESLA-type) linear collider offers some advantages over an X-band machine (see Section 15). However, in contrast to a compact, high-gradient X-band accelerator, a collider based on the current TESLA-type design would be characterized by low accelerating gradients, damping rings whose length (a few kilometers in circumference) limits the luminosity of the machine, and a technologically challenging cryogenic system that requires a number of surface cryogenic plants. Furthermore, the electron bunches in a TESLA-type machine are considerably longer than in an X-band linac, which means that much more powerful laser pulses are needed to achieve comparable photon densities at the Compton interaction region. But the most serious drawback, in our opinion, of the TESLA-type design is that it cannot be used as a prototype for a high-gradient, TeV-scale linear collider such as CLIC.

## Acknowledgements

The study of high-gradient rf structures mentioned in Section 10 of this proposal was initiated by the CLIC collaboration, and has been conducted at CERN, KEK and SLAC. We greatly appreciate the support we have received from W. Wuensch and his colleagues at CERN, and from S. Tantawi and his collaborators at SLAC.

We are also grateful to K. Flöttmann, K. Fujii, S. Fukuda, S. Hiramatsu, G. Jikia, S. Kazakov, K. Kubo, S. Matsumoto, A. Miyamoto, K. Oide, Y. Okada, A. Seryi, D. Sprehn, N. Toge, A. Wolski and K. Yokoya for their help with regard to various aspects of this proposal.

## References

- [1] GLC Project Report, K. Abe et al. (2003).
- [2] The LEP Collaborations, R. Barate et al., Phys. Lett. B **565**, 61 (2003).
- [3] J. Erler et al., Phys. Lett. B **486**, 125 (2000).
- [4] H. E. Haber and R. Hempfling, Phys. Rev. Lett. **66**, 1815 (1991); Y. Okada, M. Yamaguchi and T. Yanagida, Prog. Theor. Phys. **85**, 1 (1991); J. R. Ellis, G. Ridolfi and F. Zwirner, Phys. Lett. B **257**, 83 (1991).
- [5] M. Carena et al., Phys. Lett. B **355**, 209 (1995); M. Carena, M. Quiros and C. Wagner, Nucl. Phys. B **461**, 407 (1996); H. E. Haber, R. Hempfling and A. Hoang, Z. Phys. C **75**, 539 (1997); S. Heinemeyer, W. Hollik and G. Weiglein, Eur. Phys. J. C **9**, 343 (1999); G. Degrandi et al., Eur. Phys. J. C **28**, 133 (2003).
- [6] J. J. van der Bij, Nucl. Phys. B **267** (1986) 557.
- [7] E. Boos et al., Nucl. Instrum. Meth. A **472**, 100 (2001).
- [8] R. Belusevic, *Low-Energy Photon Collider*, KEK Preprint 2003-2 (2003).
- [9] M. Mühlleitner et al., DESY 00-192; hep-ph/0101083 (2001).
- [10] B. Grzadkowski and J. Gunion, Phys. Lett. B **294**, 361 (1992).
- [11] K. Hagiwara, Nucl. Instrum. Meth. A **472**, 12 (2001).
- [12] K. Abe et al., GLD Detector Outline Document (2006).
- [13] S. Heinemeyer et al., CERN-PH-TH/2005-228; hep-ph/0511332.
- [14] U. Baur, T. Plehn and D. L. Rainwater, Phys. Rev. D **68**, 033001 (2003).
- [15] R. Belusevic and G. Jikia, Phys. Rev. D **70**, 073017 (2004); hep-ph/0403303.
- [16] A. Djouadi et al., Eur. Phys. J. C **10**, 27 (1999).
- [17] D. J. Miller and S. Moretti, Eur. Phys. J. C **13**, 459 (2000).
- [18] C. Castanier et al., hep-ex/0101028.
- [19] G. Belanger et al., Phys. Lett. B **576**, 152 (2003).
- [20] R. Belusevic, *A 160–320 GeV linear collider to study  $e^+e^- \rightarrow HZ$  and  $\gamma\gamma \rightarrow H, HH$* , KEK Preprint 2008-33 (2008); arXiv:0810.3187v2 (2009).
- [21] G. Jikia, Nucl. Phys. B **412**, 57 (1994).
- [22] I. Ginzburg et al., Nucl. Instrum. Meth. **219**, 5 (1984).
- [23] S. Kawada et al., Phys. Rev. D **85**, 113009 (2012).
- [24] J. Tian, K. Fujii and Y. Gao, arXiv:1008.0921v2 (2010).
- [25] D. Asner et al., Eur. Phys. Journal C **28**, 27 (2003).
- [26] K. Fujii, T. Matsui and Y. Sumino, Phys. Rev. D **50**, 4341 (1994).

- [27] R. D. Ruth, Proceedings of the 2001 Particle Accelerator Conference, Chicago.
- [28] C. Adolphsen, *Advances in Normal Conducting Accelerator Technology from the X-band Linear Collider Program*, SLAC-PUB-11224, and Proceedings PAC-2005.
- [29] J. Ellis and I. Wilson, *Nature* **409**, 431–435 (18 January 2001).
- [30] CLIC Conceptual Design Report, CERN 2012-XXX and KEK Report 2012-2.
- [31] T. Higo et al., *Characteristics of Vacuum Breakdowns Under High Gradient Pulsed Operation*, THPS093, PASJ12, Ann. Meeting Part. Accel. Soc. Japan, Osaka, August 2012.
- [32] T. Ogitsu et al., SLAC-REPRINT-1995-015 (1995).
- [33] D. Sprehn et al., SLAC-PUB-11162 (2004).
- [34] P. Csonka, *Phys. Lett. B* **24**, 625 (1967); CERN Yellow Report TH 772 (1967).
- [35] I. Ginzburg et al., *Nucl. Instrum. Meth.* **205**, 47 (1983).
- [36] V. Telnov, *Acta Phys. Pol. B* **37**, 1049 (2006).
- [37] B. Badalek et al., *Int. J. Mod. Phys.* **19**, 5097 (2004).
- [38] E. Saldin, E. Schneidmiller and M. Yurkov, *Nucl. Instrum. Meth. A* **472**, 94 (2001); E. Saldin et al., SLAC-PUB-13768 (2009).
- [39] P. Michelato, Proc. EPAC08, Genoa (2008); K. Flöttmann, private communication.
- [40] ILC Reference Design Report, G. Aarons et al. (2007).
- [41] K. Skulina et al., *The Future of Particle Physics*, Snowmass Conf. 2001.
- [42] J. Gronberg, ALC Workshop, SLAC (2004).
- [43] B. Parker et al., Proc. 2007 Part. Accel. Conf., Albuquerque; SLAC-PUB-12832 (2007).
- [44] L. Shekhtman and V. Telnov, physics/0411253.
- [45] P. Emma and T. Raubenheimer, *Phys. Rev. STAB*, Vol. **4**, 021001 (2001).
- [46] A. Pak et al., BUDKER-INP 2003-7; hep-ex/0301037.
- [47] F. Bechtel et al., *Nucl. Instrum. Meth. A* **564**, 243 (2006).